Key Points:
- The atmospheric forcing in the Gulf of Mexico is highly seasonal: weak forcing in the summer alternates with strong forcing in the winter
- Synoptic-scale variability dominates in the winter; the diurnal cycle is more pronounced in the summer
- The new UWIN-CM model captures essential air-sea processes and produces skillful ocean/weather forecasts under a wide range of conditions

Atmospheric forcing of the upper ocean transport in the Gulf of Mexico: From seasonal to diurnal scales

Falko Judt[1,2], Shuyi S. Chen[1], and Milan Curcic[1]

[1]Department of Ocean Sciences, Rosenstiel School of Marine and Atmospheric Science, University of Miami, Miami, Florida, USA, [2]Now at Mesoscale and Microscale Meteorology Laboratory, Atmospheric Center for Atmospheric Research, National Center for Atmospheric Research, Boulder, Colorado, USA

Abstract The 2010 Deepwater Horizon oil spill in the Gulf of Mexico (GoM) was an environmental disaster, which highlighted the urgent need to predict the transport and dispersion of hydrocarbon. Although the variability of the atmospheric forcing plays a major role in the upper ocean circulation and transport of the pollutants, the air-sea interaction on various time scales is not well understood. This study provides a comprehensive overview of the atmospheric forcing and upper ocean response in the GoM from seasonal to diurnal time scales, using climatologies derived from long-term observations, in situ observations from two field campaigns, and a coupled model. The atmospheric forcing in the GoM is characterized by striking seasonality. In the summer, the time-average large-scale forcing is weak, despite occasional extreme winds associated with hurricanes. In the winter, the atmospheric forcing is much stronger, and dominated by synoptic variability on time scales of 3–7 days associated with winter storms and cold air outbreaks. The diurnal cycle is more pronounced during the summer, when sea breeze circulations affect the coastal regions and nighttime wind maxima occur over the offshore waters. Realtime predictions from a high-resolution atmosphere-wave-ocean coupled model were evaluated for both summer and winter conditions during the Grand LAgrangian Deployment (GLAD) in July–August 2012 and the Surfzone Coastal Oil Pathways Experiment (SCOPE) in November–December 2013. The model generally captured the variability of atmospheric forcing on all scales, but suffered from some systematic errors.

1. Introduction

The Gulf of Mexico (GoM) is a semiclosed ocean basin surrounded by the North American continent. Due to its geographic location, the GoM is subjected to a wide range of atmospheric conditions, which play a dominant role in the basin's upper ocean circulation. One particular characteristic of the GoM's climate is its striking seasonality, giving rise to a broad spectrum of atmospheric phenomena from hurricanes to winter storms. Recently, the Deepwater Horizon oil spill of 2010 and the Hercules fire of 2013 have highlighted the importance of studying the atmosphere and ocean as a coupled system to better understand their integrated effects on lower atmospheric and upper ocean transports. Atmosphere and ocean are closely coupled from seasonal to diurnal time scales, warranting a comprehensive overview of the multiscale atmospheric forcing and upper ocean response.

Earlier work has mostly focused on atmospheric forcing on seasonal or longer time scales, because the coupling between the ocean and atmosphere is an important aspect of the GoM's climate system [*de Velasco and Winant*, 1996; *Wang et al.*, 1998; *Zavala-Hidalgo et al.*, 2014]. *Zavala-Hidalgo et al.* [2014] showed that the wind forcing undergoes a seasonal cycle with weaker winds during the summer and stronger winds during the winter. In agreement with the seasonal wind speed cycle, waves are considerably higher in the winter [*Appendini et al.*, 2014]. In the summer, the wind stress curl is negative (anticyclonic) north of 23°N and positive (cyclonic) south of that latitude, mainly in the Campeche Bay. Due to a shift in the large-scale wind patterns, the zero line of the wind stress curl is displaced northward during the winter [*de Velasco and Winant*, 1996]. The stronger wintertime forcing also causes the mixed layer to deepen from an average of $\sim$ 20 m in July to 75 m in February [*Mendoza et al.*, 2005].

Previous studies suggest that when the trade winds in the Caribbean Sea weaken from summer to fall, conditions become more favorable for the Loop Current to shed an anticyclonic ring [*Chang and Oey*, 2012; *Xu et al.* 2013]. Using idealized model experiments, *Chang and Oey* [2010a] showed that wind forcing in the

GoM basin could also affect the frequency of Loop Current eddy shedding events, the size of Loop Current eddies, and introduce an eastward upper layer flow over the deep central basin toward the Loop Current. In addition, a steady, westward mean wind would increase the upper ocean heat content in the GoM significantly [*Chang and Oey*, 2010b]. However, the aforementioned studies were not able to investigate the effects of realistic atmospheric variability on shorter-time scales. Wind forcing furthermore plays an important role in the dynamics of the inner GoM shelves, where westward winds are responsible for the buoyant waters from the Mississippi River to spread onto the Louisiana-Texas Shelf [*Oey*, 1995].

The atmospheric forcing of the upper ocean on shorter-time scales is related to distinct synoptic-scale weather systems, such as hurricanes, midlatitude cyclones (autumn and winter storms), and cold air outbreaks. The ocean response to these atmospheric phenomena has mostly been documented in observational case studies of single events [e.g., *Nowlin and Parker*, 1974; *Jaimes and Shay*, 2009; *Villanueva et al.*, 2010; *Jaimes et al.*, 2011]. Hurricanes, which usually occur from June to October, are one of the most distinct phenomena of the coupled air-sea system and a major factor in the upper ocean forcing. They interact strongly with the upper ocean in many complex ways: (1) warm water provides the energy for sustaining the storms through enthalpy fluxes, (2) the ocean acts as a sink for the momentum of the strong winds, and (3) wind-induced surface waves strongly affect the currents and upper ocean transport [*Chen and Curcic* 2015; *Curcic et al.* 2016]. Strong currents, upwelling and mixing cause regions of significantly reduced SST (cold wakes), which haven been studied extensively [e.g., *Price*, 1981; *Price et al.*, 1994; *Lee and Chen*, 2012, 2014]. Although hurricanes are extreme forcing events, they occur infrequently and irregularly, especially in the GoM. Based on data from 1949 to 2008, the GoM is on average impacted by two hurricanes annually [*Levinson et al.*, 2009]. With a return frequency of 2.5 years, major hurricanes (category 3 or higher, maximum winds $>= 50$ m s^{-1}) occur even less frequently. Ocean surface waves significant wave height (SWH) > 10 m are exclusively associated with strong hurricanes, e.g., Hurricanes Ivan (2004) and Ike (2008) [*Smith et al.*, 2013; *Chen and Curcic*, 2015]. However, these extreme waves are so rare they do not project onto the long-term mean SWH fields [*Appendini et al.*, 2014].

During the winter, synoptic-scale weather systems, especially cold fronts, are potent forcing mechanisms. *Villanueva et al.* [2010] showed that SST in the western GoM can decrease by 0.8–1.6°C due to a single cold air outbreak. These short-term decreases in SST along the shelves can be even more dramatic at times and reach values around 5°C [*Nowlin and Parker*, 1974]. The deepening of the mixed layer during the winter is primarily associated with stronger winds and vertical entrainment of colder water, whereas sensible heat fluxes and horizontal advection by eddies/currents play a secondary role [*Villanueva et al.*, 2010]. *Nowlin et al.* [2005] documented that the circulations on the inner Texas-Louisiana continental shelf is dominated by variability on time scales of 2–10 days, which is consistent with synoptic-scale atmospheric forcing.

The overall goal of this paper is to investigate the atmospheric forcing and upper ocean response in the GoM on seasonal, synoptic, and diurnal scales. A better understanding of the multiscale atmospheric forcing in the GoM is crucial for the interdisciplinary effort of predicting pathways of pollutants during the potential future oil spills. We use climatologies to illustrate the seasonal cycle, and highlight the variability on shorter-time scales with collocated atmosphere-ocean observations and coupled model predictions. The comprehensive overview of the multiscale variability provides a larger context for the observations from past and future field experiments. This study also reports on the evaluation of a newly developed coupled atmosphere-ocean-wave model with a particular emphasis on model biases that are relevant for its energetic consistency.

The paper is organized as follows: in section 2, we present climatologies of various oceanic and atmospheric variables with focus on the seasonal cycle and how it modulates the atmospheric forcing. Section 3 introduces two field experiments, which were designed to better understand the distinct seasonal variability in the GoM, and the coupled model. Section 4 provides on overview of the atmospheric and oceanic conditions during the field experiments using model and observations, emphasizing the synoptic-scale variability. The diurnal cycle and its spatiotemporal variability in the GoM are analyzed in section 5. Finally, the summary and conclusions are given in section 6.

2. Climatological Conditions and Seasonal Variability

2.1. Data

The climatology of the GoM coupled system is best studied with long-term observations from remote sensing and in situ observing systems. In this study, we use the 0.1°-resolution REMSS Merged SST product and
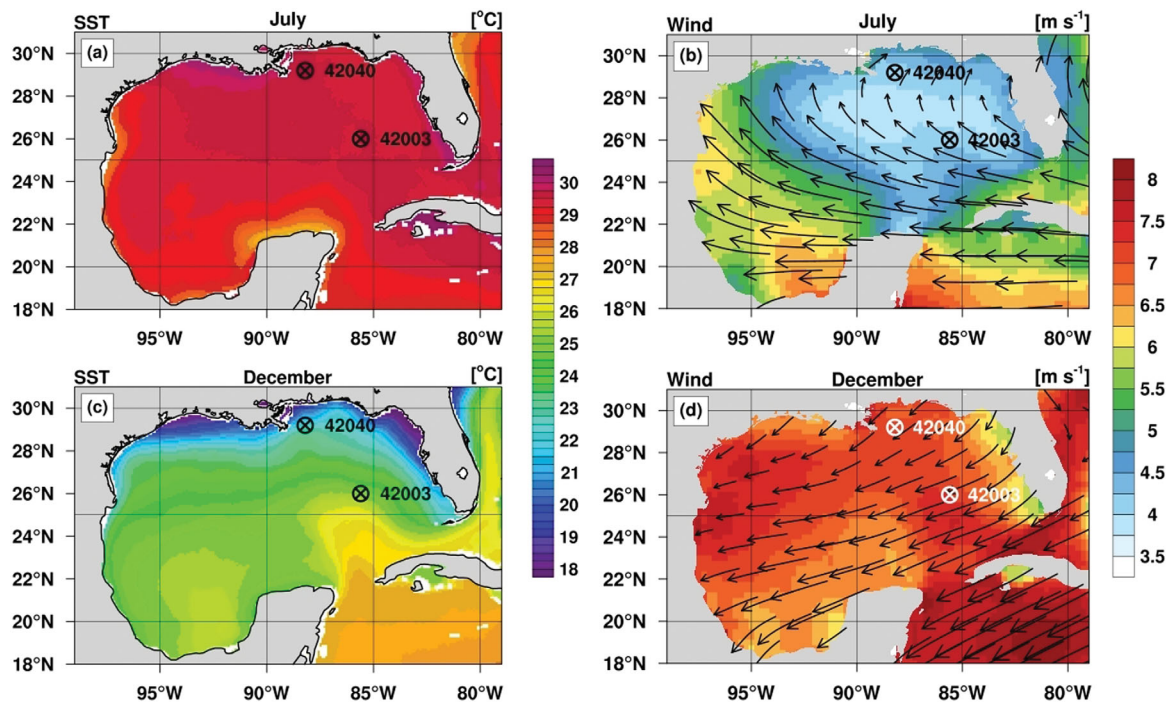
Figure 1. Long-term (2002–2013) monthly (left) mean SST and (right) winds in (top) July and (bottom) December.

the 0.25°-resolution NOAA Sea Winds products, each based on 2002–2013 data. Hourly observations from NOAA National Data Buoy Center (NDBC) Stations 42003 (1976–2014) and 42040 (1995–2014) provide the foundation for a detailed climatology of several collocated atmospheric and oceanic variables. We chose these two sites (marked in Figure 1) to highlight the climatological differences between the nearshore and offshore environment.

2.2. Annual Cycle and Summer/Winter Mean Conditions

The SST maps (Figures 1a and 1c) and buoy temperature data (Figures 2a–2d) illustrate the spatiotemporal variability of water and air temperature. During the summer, the uniformly high SST (29–30°C) mask dynamical features such as the Loop Current (Figure 1a). In contrast, the mean December SST reflects the mean structure of the Loop Current and the GoM bathymetry (lower temperatures along the northern shelves; Figure 1c). Both air and water temperature exhibit an archetypical annual cycle, and reach their climatological extrema in late July/early August late January/early February (Figures 2a–2d). Due to the lower thermal inertia of the shallow coastal waters and the distance to the warmer Loop Current, SST cools more drastically along the northern coast in the winter. The amplitudes of the annual air and water temperature cycles near the shore are approximately twice as large as offshore (Figures 2a–2d).

The strong seasonality of the atmospheric forcing in the GoM is associated with a seasonal shift in the large-scale atmospheric flow pattern (Figures 1b and 1d). The climatological mean wind speed reaches its minimum in midsummer (Figures 2e and 2g), when the northeastern GoM is dominated by light, anticyclonic flow featuring magnitudes of < 5 m s^{-1}. Winds increase during the fall and remain elevated in the central GoM throughout the winter until midspring, without a clear maximum (Figure 2g). Closer to the northern shore, the annual wind speed cycle features a more distinct peak at the turn of the year (Figure 2e). The seasonal variability in SWH closely mirrors the annual wind speed cycle (Figures 2f and 2h); median wave heights are maximum in midwinter (~ 1.2 m), and decrease to ~ 0.5 m during the summer. Except for the more pronounced midwinter wind speed peak at Station 42040, differences in terms of wind speed/ SWH are minor between the nearshore and offshore site.

The anticyclonic wind pattern during the summer (Figure 1b) is due to a branch of the subtropical high-pressure system centered over the western North Atlantic. While most of the GoM is dominated by easterly/southeasterly flow, winds turn to southwesterly directions north of the high-pressure axis around 28°N
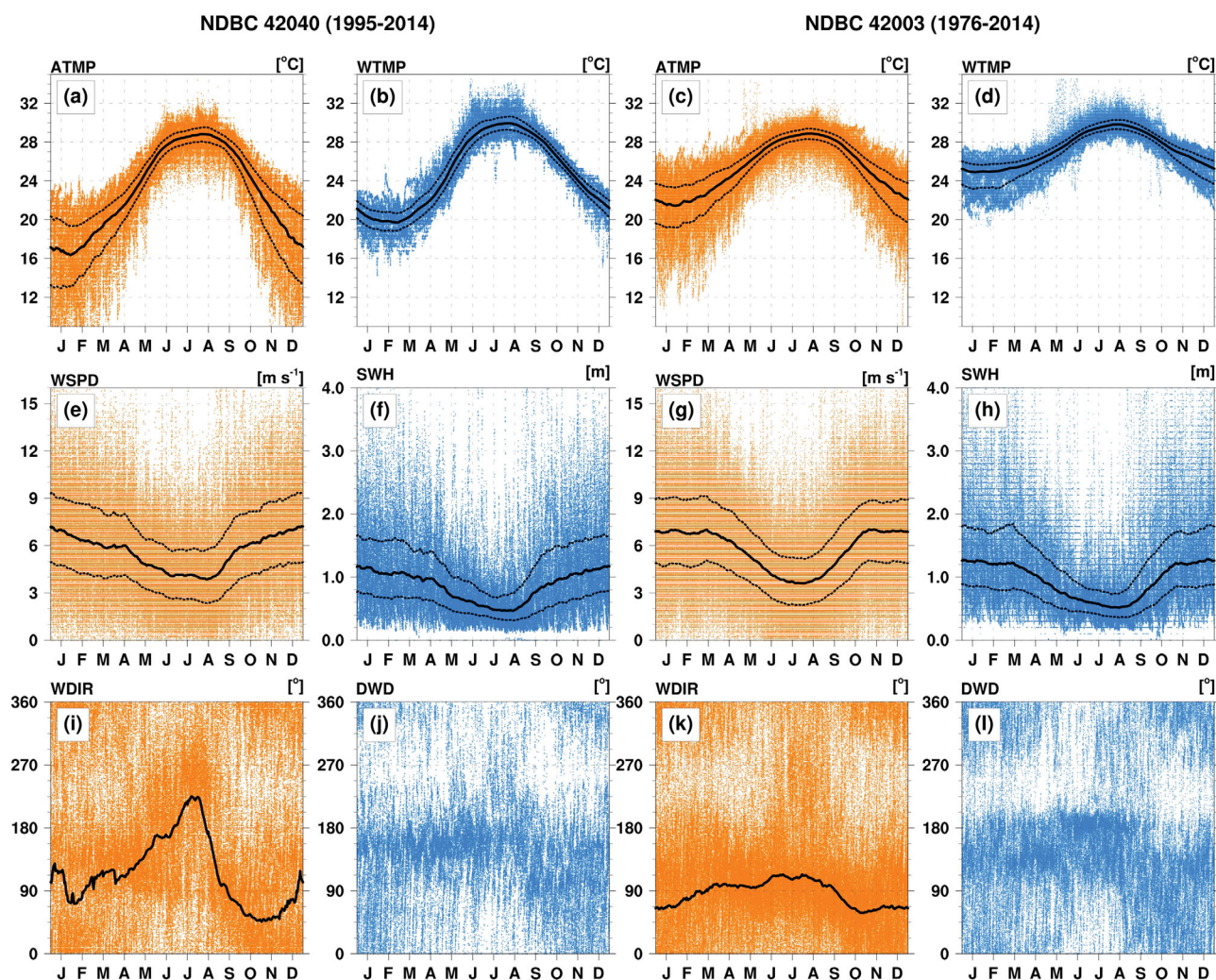
NDBC 42040 (1995-2014)   **NDBC 42003 (1976-2014)**

Figure 2. Annual cycles of various (orange) atmospheric and (blue) ocean variables from NDBC Station (left two columns) 42040 and (right two columns) 42003. Atmospheric variables: air temperature (a, c), wind speed (e, g), and wind direction (i, k). Ocean variables: water temperature at 0.6 m depth (b, d), significant wave height (f, h), and dominant wave direction (j, l). Wind direction and dominant wave direction denote the direction wind/waves are coming from (standard meteorological convention). In Figures 2a–2h, thick black lines highlight the medians and thin lines the interquartile range (25th and 75th percentiles). The black lines in Figures 2i and 2k denote the wind vector average. There are no lines in Figures 2j and 2l, because the NDBC data does not allow for computing a wave direction vector average.

(Figure 1b). In the winter, the large-scale pattern changes considerably, and the anticyclonic flow disappears. Along the northern coast, the climatological wind direction undergoes a distinct seasonal shift, and reverses by almost 180° from southwesterly (onshore) during the summer to northeasterly directions (offshore) in the winter (Figures 1d and 2i). At NDBC Station 42003 in the east-central Gulf, the seasonal wind shift is subtler (Figure 1k). The seasonal variability in the dominant wave direction is less pronounced than the seasonal shift in wind direction, and only features little qualitative differences between the two sites (Figures 1j and 1l). Dominant waves that propagate from southeast to northwest prevail throughout the year, but especially during the winter, dominant waves also arrive from northerly directions. In general, there is very little wave activity propagating from southwest to northeast, in agreement with the relative lack of southwesterly winds over the offshore waters.

2.3. Seasonal Variability of the Atmospheric Forcing

In addition to the seasonal change of the mean wind (Figures 1 and 2), the seasonal cycle also modulates the variability of the atmospheric forcing. Synoptic-scale variability is generally much more pronounced in the winter. *DiMego et al.* [1976] showed that the time period from December to March features the most frequent occurrences of midlatitude (frontal) weather systems in the GoM. In December, there are on average
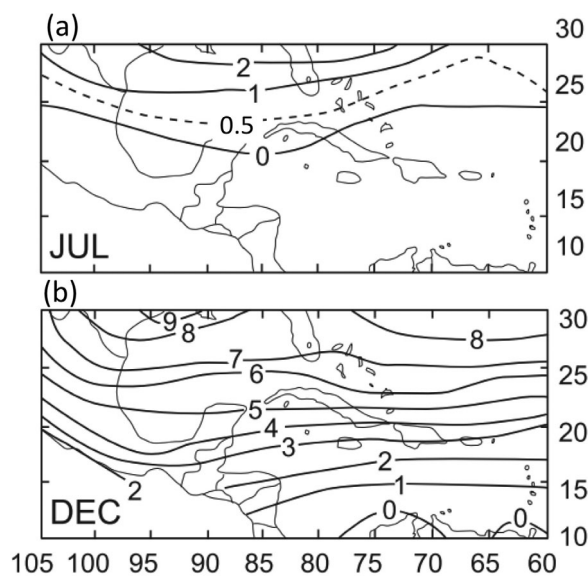
Figure 3. Monthly-mean frequency of frontal systems in (a) July and (b) December for the 1965–1972 period, expressed as the number of frontal passages per month [from *DiMego et al.*, 1976, Figure 1].

8–9 frontal incursions into the northern GoM (Figure 3b), a number that is about five times higher than in July (Figure 3a). The number and intensity of fronts decreases toward lower latitudes, and the southern GoM is usually free of frontal activity in the summer.

Winter storm activity manifests as increased variability of the variables displayed in Figure 2. For example, the interquartile range of air temperature at NDBC Station 42040 ranges from $<2°C$ in July to $\sim 8°C$ in January. The variability of SWH also features a pronounced annual cycle, and the interquartile range increases by a factor of two from summer to winter. The frequency analysis of wind speed and SWH for the summer (June–August) and winter (December–February) season in Figure 4 further illustrates the seasonality of the atmospheric forcing. We only show the frequency analysis for Station 42003, because qual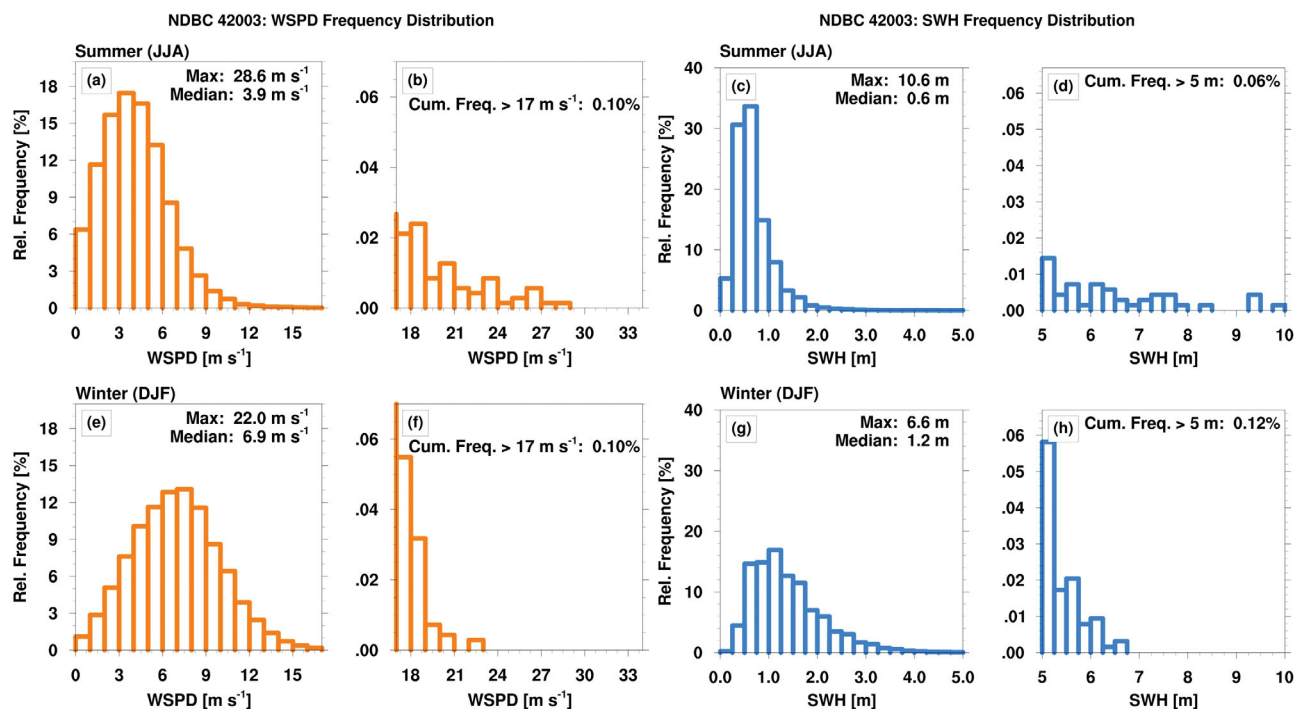itative differences between the two locations are minor. In comparison to the summer frequency distributions (Figure 4, top), the wintertime distributions are much broader and shifted to higher wind and wave magnitudes (Figure 4, bottom), which is a direct response to increased synoptic-scale variability. In both cases, the median value increases approximately by a factor of two from summer to winter. During the summer, light flow prevails and wind speeds < 5 m s^{-1} account for 67% of all observations. In the winter, winds remain below the 5 m s^{-1} threshold only 30% of the time. The seasonal contrast is even more pronounced in terms of wave activity: SWH >1 m account for only 14% of the observations in the summer, but 64% in the winter.

2.4. Extreme Winds and Waves

At any given location, wind speeds of >17 m s^{-1} (gale force and higher), and SWH > 5 m are relatively uncommon. Winds above gale force account for only 0.10% of all data points at NDBC Station 42003 during both the 3 month summer and winter periods (Figures 4b and 4f). Significant wave heights of >5 m are very rare in the summer (0.06%, Figure 4d), but occur twice as frequently in the winter (0.12%, Figure 4h). Note that the shape of the high-end tails differs between the seasons: flat and long in the summer (Figures 4b and 4d) versus a more abrupt drop-off in the winter (Figures 4f and 4h). Extreme winds of near 30 m s^{-1} and waves of 10 m height are caused by hurricanes, which only occur from June to November. The rarity of these events is reflected by the fact that Station 42003 has recorded hurricane-force winds (>32 m s^{-1}) only twice since 1976. In contrast, winds and waves associated with winter storms are less extreme (<25 m s^{-1}, <7 m), but occur more frequently.

The number of hurricanes in the GoM is modulated by the El Niño Southern Oscillation (ENSO), and while El Niño years are generally less active, La Niña years feature more frequent and stronger hurricanes [*Gray*, 1984]. Winter storm activity is also modulated by ENSO. During El Niño years, the midlatitude storm tracks are shifted further south and the storms tend to be more intense [*Eichler and Higgins*, 2006]. The long-term wind observations from Station 42003 reflect this relationship: the wind speed reached at least 17 m s^{-1} during 20 out of 36 winter seasons. Fourteen of these "active" winters coincided with a positive ENSO phase, but only two occurred during a negative phase, and two during neutral conditions.

3. Field Experiments and Real-Time Model Predictions

3.1. Background

The Deepwater Horizon accident in the GoM was a major ecological and economical disaster, which stimulated an interdisciplinary effort to accurately predict the fate of hydrocarbon released into the environment

Figure 4. Frequency distributions of wind speed (a–b, e–f) and significant wave height (c–d, g–h) based on the data in Figures 1g–1h. (top) Summer season (June–August); (bottom) winter season (December–February).

and its ecological consequences. As an integral part of this research, the Consortium for Advanced Research on Transport of Hydrocarbon in the Environment (CARTHE) studies the physical distribution and dispersion of petroleum and its constituents [*Özgökmen et al.*, 2014]. The ultimate goal of the consortium is to accurately predict the propagation of hydrocarbon using newly developed models. While it is generally known that the surface wind is an important driver of the upper ocean circulation, the actual transport and dispersion of oil depend on a large number of multiscale and complex processes along the air-sea interface. The dominant mechanisms of oil dispersion, such as wind-wave mixing and surface layer transport from the open ocean to coastal areas, involve atmospheric and oceanic interactions on scales that span six orders of magnitudes, many of which are not well understood. Furthermore, current models poorly simulate physical processes of the air-sea interface that determine the ocean response to atmospheric forcing. For example, most numerical models do not explicitly simulate the exchange of momentum through wave growth and dissipation. Recent research shows, however, that accurate predictions of upper ocean dynamics are only possible when the air-sea exchange of momentum and enthalpy is simulated realistically [*Chen et al.*, 2007, 2013; *Lee and Chen*, 2012].

3.2. The GLAD and SCOPE Field Campaigns

Two field programs, the Grand LAgrangian Deployment (GLAD) [*Poje et al.*, 2014; *Coelho et al.*, 2015] and the Surfzone Coastal Oil Pathways Experiment (SCOPE), were designed to better understand the distinct seasonal variability of the atmospheric forcing in the GoM. GLAD was intended to study mesoscale ocean currents and their role in dispersing pollutants, and took place in the northeastern GoM during July and August 2012. With more than 300 drifters released in the open waters, GLAD was the largest dispersion experiment of its kind [*Özgökmen et al.*, 2014; *Poje et al.*, 2014]. In addition to the large number of passive ocean surface drifters, CARTHE deployed four Surface Velocity Project Barometer (SVPB) [*Sybrandy et al.*, 2009] and three MINIMET buoys, which were able to measure atmospheric conditions, collocated with sea surface temperature. Autonomous Drifting Ocean Stations (ADOS) drifters measured the ocean temperature at various depths.

SCOPE was a nearshore field experiment conducted in November and December 2013, and focused on smaller-scale processes under stronger wintertime forcing. A particular emphasis during SCOPE was placed
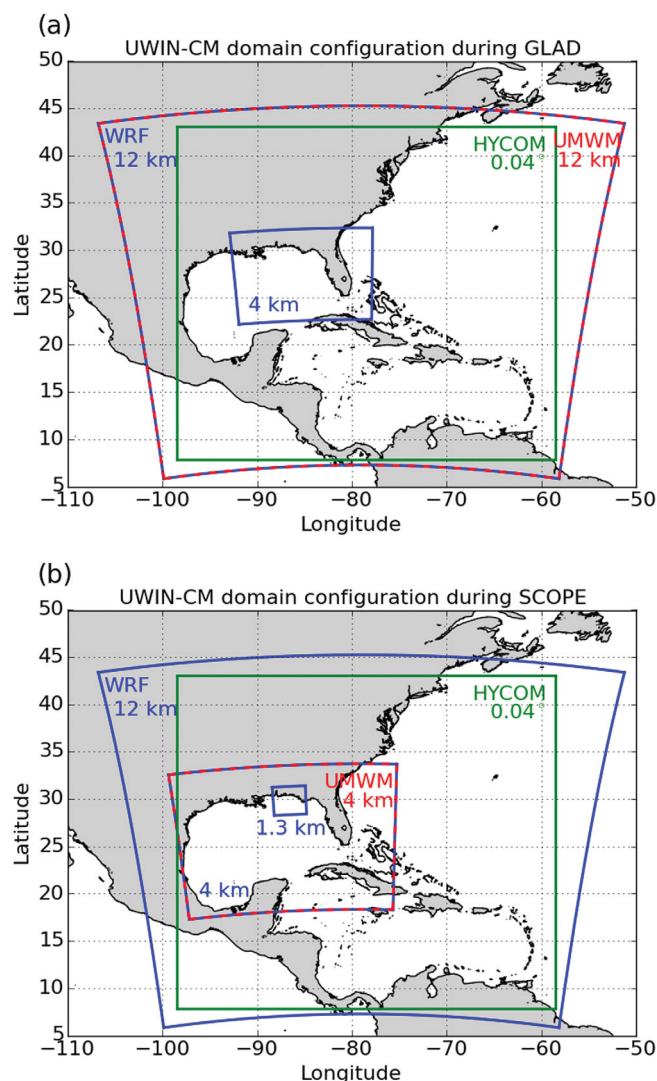
Figure 5. UWIN-CM domain configurations during (a) GLAD and (b) SCOPE.

on the cross-shore exchange of material between the inner shelf and the surf zone. During both experiments, atmospheric variability on synoptic and diurnal time scales influenced the upper ocean transport and temperature distribution substantially.

3.3. The Coupled Atmosphere-Wave-Ocean Model

Because the lower atmosphere and air-sea interaction play a dominant role in the dynamics of the upper ocean, a new high-resolution, fully coupled atmosphere-wave-ocean model has been developed to study air-sea processes in a unified framework. This model explicitly accounts for atmosphere-ocean momentum exchange through surface waves using the Unified Wave INterface (UWIN), and is therefore termed the UWIN-Coupled Model (UWIN-CM) [*Chen and Curcic*, 2015]. In addition to better understanding the complex processes of the air-sea interface, UWIN-CM was also used for realtime weather predictions during GLAD and SCOPE [*Curcic et al.*, 2016]. The daily forecasts of atmospheric and oceanic conditions helped the scientists the field to execute the experiments successfully.

The specifics of the model and its setup are described in *Chen and Curcic* [2015] and *Curcic et al.* [2016].

Here, we only list the most important information. During GLAD (Figure 5a), the atmospheric component was configured with an outer domain (12 km grid spacing), which covered the GoM, the Caribbean Sea, a large portion of the United States, and parts of the western Atlantic Ocean. A nested domain with 4 km grid spacing, centered on the northern GoM coast, covered the eastern half of the GoM and Florida. During SCOPE (Figure 5b), the setup was similar, but the 4 km domain was enlarged to encompass the entire GoM and a third nested domain with 1.3 km grid spacing was centered on the location of the experiment in the western Florida panhandle. The Hybrid Coordinate Model (HYCOM) served as the ocean component of the coupled model, covering the GoM, Caribbean Sea and western Atlantic with a resolution of 0.04°.The wave model was the University of Miami Wave Model (UMWM) [*Donelan et al.*, 2012] with 4 km resolution.

During the realtime experiments, UWIN-CM was initialized once per day at 00:00 UTC and integrated for 72 h. Initial and lateral boundary conditions for the atmospheric and ocean components came from the Global Forecast System (GFS) and HYCOM, respectively. In total, UWIN-CM produced 35 forecasts during GLAD (22 July to 26 August 2012) and 23 forecasts during SCOPE (25 November to 18 December 2013, no forecast on 26 November 2013). For the analysis and model evaluation in this paper, we follow the method of *Chen and Curcic* [2015] and use model predictions from the t = 24–48 h forecast time period.
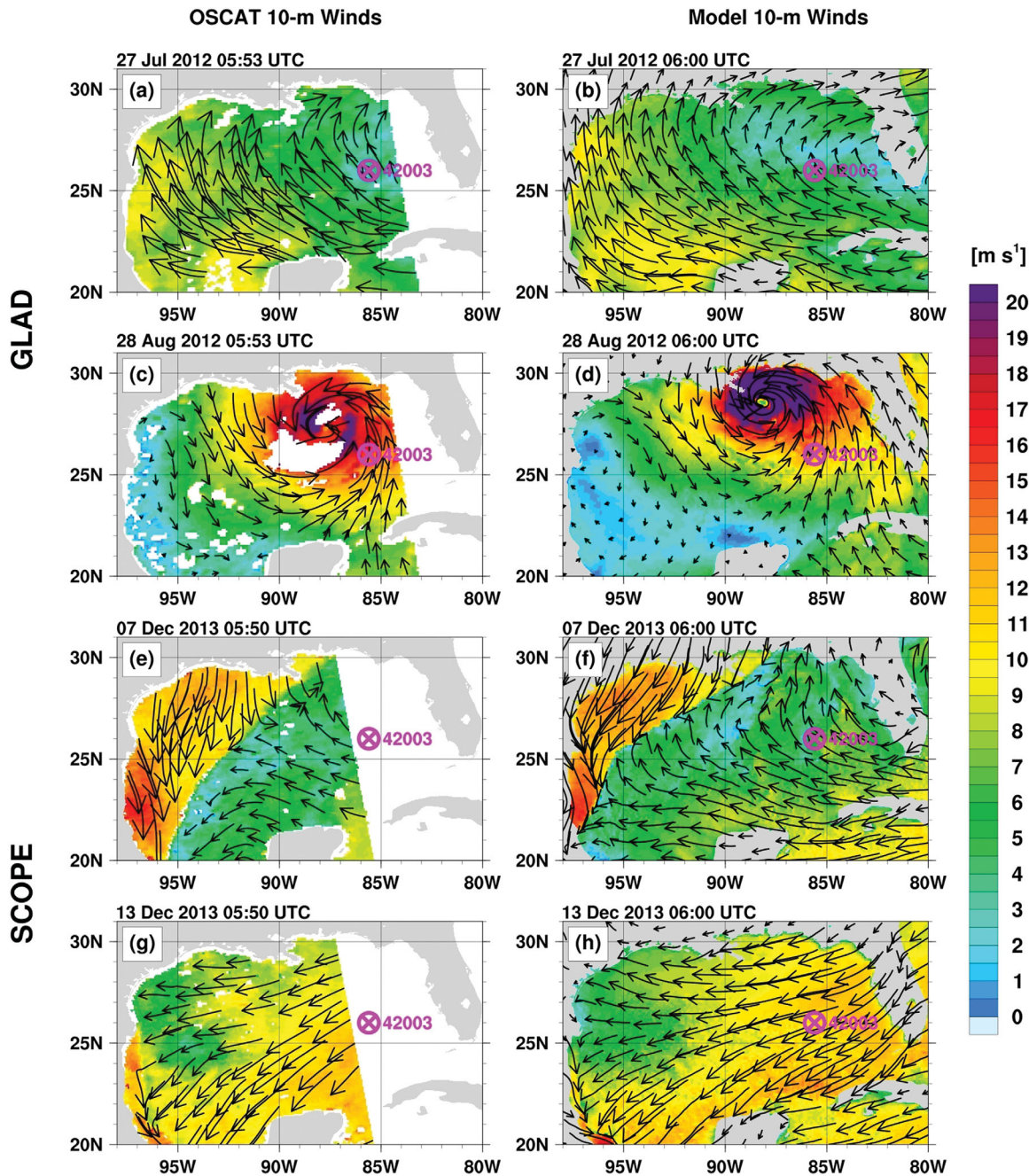
Figure 6. Snapshots of 10 m winds during (a–d) GLAD and (e–h) SCOPE. (left) Oceansat-2 scatterometer winds; (right) Corresponding 30 h UWIN-CM wind predictions.

4. Atmospheric Forcing During GLAD and SCOPE

4.1. General Overview

In agreement with the climatological analysis in section 3, the atmospheric conditions during GLAD (summer) and SCOPE (winter) differed considerably. The atmospheric flow during GLAD was generally characterized by light winds, especially in the northeastern GoM, which is depicted by Oceansat-2 Scatterometer (OSCAT) winds and UWIN-CM prediction in Figures 6a and 6b. The large-scale pattern resembled the climatological mean winds (Figure 1b), and featured little day-to-day variability. In a moment of scientific serendipity, Hurricane Isaac traversed the region in late August 2012 after all GLAD drifters had been deployed. With estimated maximum winds of 35 m s^{-1} [*Berg*, 2013], Isaac was the strongest atmospheric forcing event in the GoM in 2012. The storm moved across the dense array of drifters on 28 August (Figures 6c and 6d)
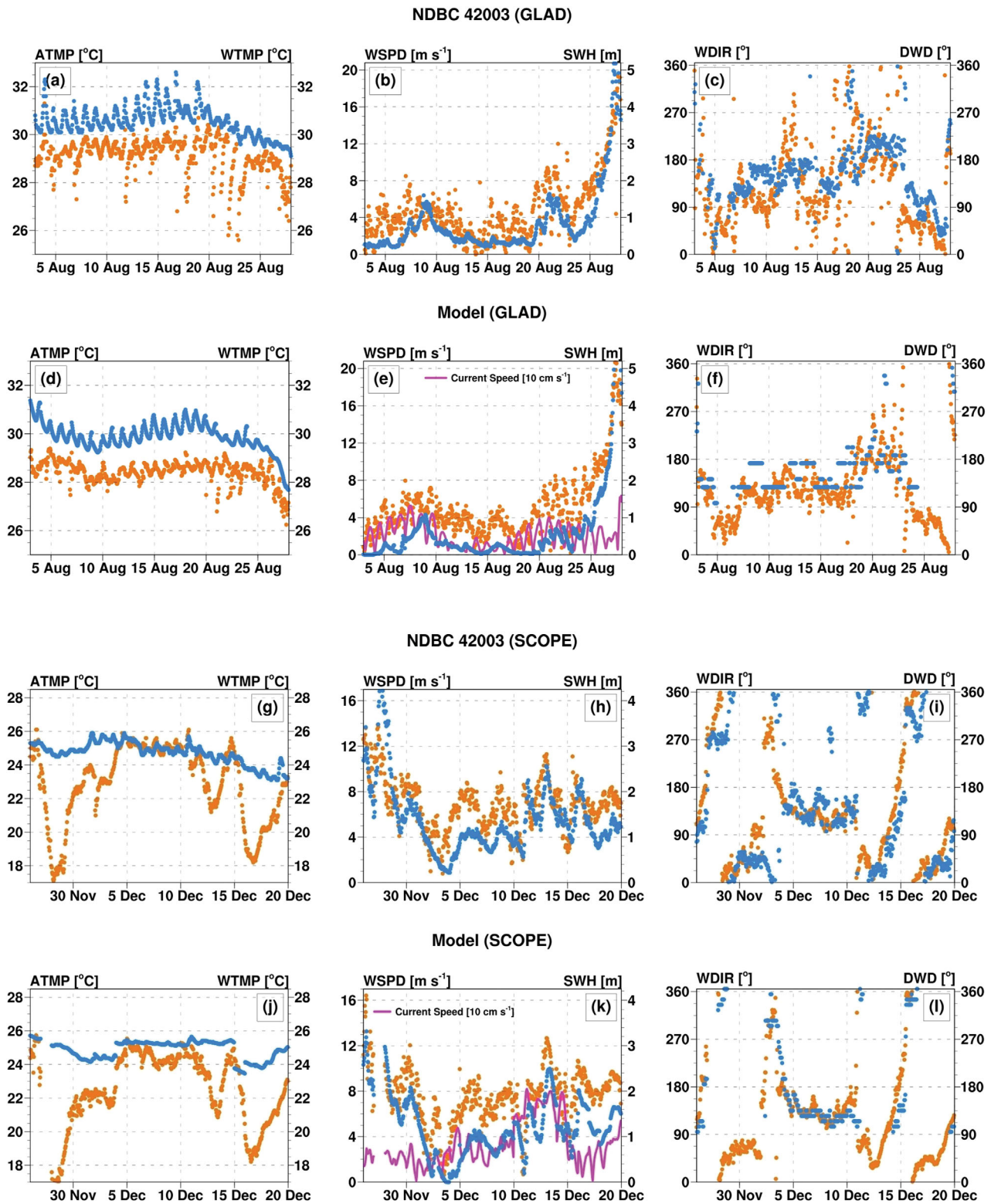
Figure 7. Time series of (orange) atmospheric and (blue) ocean variables from (a–c, g–i) NDBC Station 42003 and (d–f, j–l) the corresponding UWIN-CM predictions. (top two rows) GLAD period (1–29 August 2012); (bottom two rows) SCOPE period (26 November to 20 December 2013). Atmospheric variables: air temperature (a, d, g, j), wind speed (b, e, h, k), and wind direction (c, f, i, k). Ocean variables: water temperature (a, d, g, j), significant wave height (b, e, h, k), and dominant wave direction (c, f, i, k). Magenta lines in Figures 7e, 7k are surface current magnitudes from the UWIN-CM predictions.
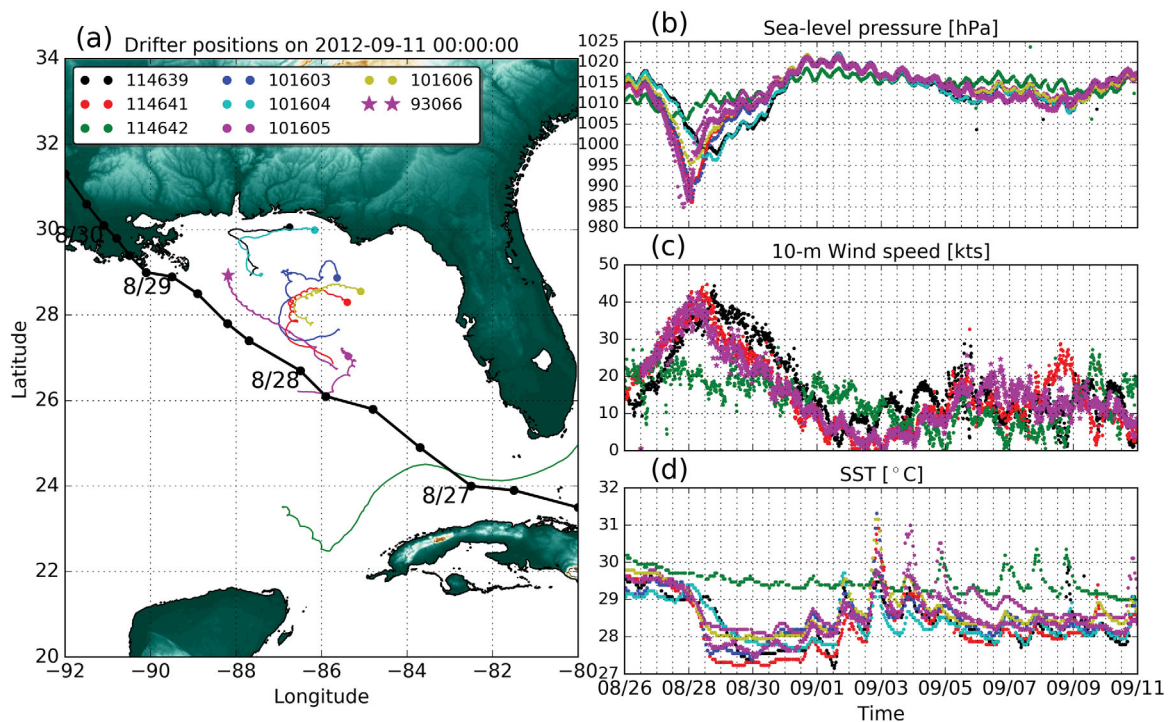
Figure 8. (a) Trajectories of MINMET and SVBP buoys and, in addition, ADOS drifter 93066 for the 00:00 UTC 26 August 2012 to 1800 UTC 7 September 2012 time period. (right plots) Drifter observations of (b) sea level pressure, (c) 10 m wind speed, and (d) SST.

[*Curcic et al.*, 2016, Figure 1], and large parts of the eastern GoM were dominated by Isaac's intense cyclonic circulation.

In contrast to the relatively steady atmospheric forcing during GLAD (excluding Hurricane Isaac), the wind forcing during SCOPE was generally stronger and more variable. The OSCAT and model winds on 7 and 13 December 2013 (Figures 6e–6h) exemplify the typical evolution of the synoptic-scale flow. A wind surge associated with an advancing cold front moved into the GoM on 7 December (Figures 6e and 6f). Behind the front, which is marked by an abrupt wind shift from easterly to northerly directions, wind speeds were in the 10–15 m s^{-1} range. A few days after the front had passed and dissipated, the flow relaxed somewhat and shifted from northerly to easterly directions (Figures 6g and 6h). This general progression repeated in irregular intervals on the order of 3–7 days with the continued development of midlatitude weather systems.

4.2. Wind and Wave Forcing and Upper Ocean Response in Model and Observations

The evolution of atmospheric and related oceanic variables from NDBC Station 42003 observations (Figures 7a–7c, 7g–7i) and model forecasts (Figures 7d–7f, 7j–7l) illustrate the variability of atmospheric forcing and ocean response during GLAD (Figures 7a–7f) and SCOPE (Figures 7g–7l). The close agreement between atmospheric (orange) and oceanic (blue) variables indicates that both atmosphere and ocean are closely coupled.

Diurnal temperature oscillations dominated much of the GLAD period (Figures 7a and 7d), especially during light wind/low wave periods (Figures 7b and 7e). Cloud cover subdued diurnal SST oscillations after 20 August, and SST decreased substantially when the wind field of Isaac approached. Large negative swings in air temperature, most noticeable between 15 and 25 August, were related to episodes of rain (Figures 7a and 7d). Beginning on 25 August, Isaac approached Station 42003 and winds steadily increased to 20 m s^{-1} over a period of a few days. In tandem with the strong winds, SWH increased to >5 m. During most of the GLAD period, the prevailing wind and dominant wave direction were from the southeast (Figures 7c and 7f), in good agreement with the climatological mean wind (Figure 1b). A distinctive change in wind/wave direction occurred when the center of Isaac moved close to the buoy's location on 27 August.
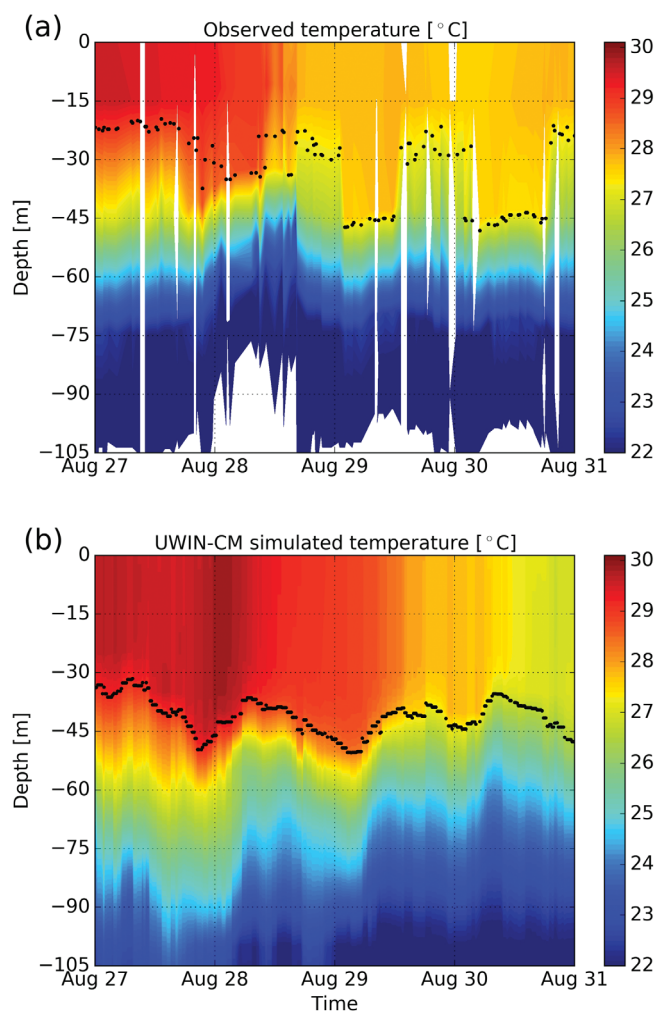
Figure 9. (color) Upper ocean temperature and (dots) mixed layer depth from (a) in situ observations by the ADOS 93066 drifter and (b) coupled atmosphere-wave-ocean model forecast sampled along the drifter trajectory during the passage of Hurricane Isaac.

Issac's passage allowed for firsthand observations of the upper ocean evolution under extreme wind conditions [*Curcic et al.* 2016]. The SVPB and MINIMET drifters gathered unique, collocated observations of oceanic and atmospheric variables during and after the hurricane's passage (Figure 8). The trajectories of the buoys between 26 August and 7 September are shown in Figure 8a. Time series of sea level pressure and wind speed (Figures 8b and 8c) clearly show the impact of the hurricane, which manifests as a drop in pressure and increase in wind speed, with a well-defined peak on 28 August. Note that even though the anemometer-equipped drifters remained outside the storm's core, they still measured strong winds of up to 45 kts (23 m s^{-1}). One drifter, MINIMET buoy 114642 (green), escaped the GoM through the Florida Strait before the cyclone developed. This device was not affected by Isaac, and thus provides an assessment of the undisturbed environment.

During and after the passage of Isaac, the drifter's SST sensors recorded a complex ocean response to the atmospheric forcing. The upper ocean response features a superposition of variability on both multiday and diurnal time scales. Isaac's strong winds caused ocean mixing and upwelling of cooler water, which manifested in a drop in SST by 1-2°C beginning on 28 August (Figure 8d). After Isaac had passed, the SST in the cold wake recovered due to insolation after 1 September. Between 1 and 5 September 2012, the winds in the northeastern GoM decreased to almost calm conditions (Figure 8c), and the buoys recorded pronounced diurnal SST oscillations with 1–2°C amplitude. This pattern can be explained as follows: during the day, insolation heated the top ocean layer and the lack of wind prevented the mixing that usually moderates SST. At night, SST cooled to 28–29°C by way of outgoing longwave radiation. The absence of mixing during this period resulted in daytime SST peaks that were actually higher than prior to Isaac's impact (31.5°C). Soon after the winds increased again to ~20 kts (10 m s^{-1}), the diurnal SST oscillations disappeared. The resumed mixing brought cooler waters from Isaac's wake to the surface, which had been masked by the very warm skin layer. MINIMET buoy 114639 (black) recorded distinct diurnal wind oscillations beginning on 1 September (Figure 8c), coinciding with the diurnal SST cycles. This buoy was located closer to the coast and therefore influenced by the land-sea breeze circulation. The other buoys farther from the coast show a much more subtle diurnal cycle, indicating that the diurnal wind forcing is strongest near the coast.

The complex upper ocean temperature response to Hurricane Isaac forcing was well captured by the ADOS 93066 drifter that moved parallel to the storm track from 27 to 31 August (Figure 8a, trajectory marked with a star symbol). The depth of the mixed layer, defined as the depth at which the temperature difference
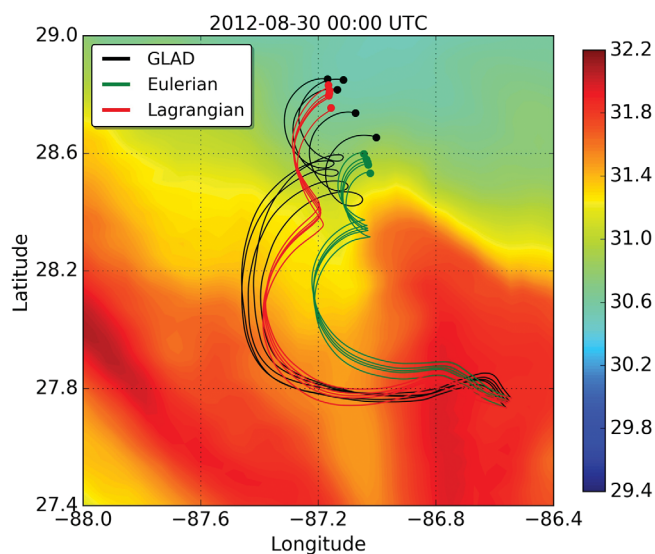
Figure 10. Trajectories of a five drifter cluster located on the right side of Hurricane Isaac from 0000 UTC 27 to 30 August 2012. The observed GLAD drifter trajectories are shown in black. UWIN-CM simulated trajectories with and without the effect of advection by waves are shown in red and green, respectively. The color background shows surface seawater density ($\times$ 1000 kg m^{-3}) simulated by the coupled model. Adapted from *Curcic et al.* [2016].

from the surface reaches 0.5°C, increased from 22 to 38 m in less than 9 h on late 27 August (Figure 9a). Strong upwelling of cold water followed on 28 August due to the Ekman divergence forced by Isaac's cyclonic winds. The drifter then captured intense inertial oscillations over the next 3 days, during which the alternating upwelling and downwelling acted to compress and stretch the mixed layer by over 20 m. The coupled model predicted the storm-induced mixing and cooling of the mixed layer (Figure 9b). However, the ocean model has a distinct bias in its initial state when the simulated mixed layer is deeper and warmer than observed, possibly due to an error in the position of a Loop Current eddy in the global HYCOM analysis fields. The inertial oscillation signal is not as prominent in the model as it is in the observations. This is likely due to the nonlocal K-profile boundary layer mixing scheme [*Large et al.*, 1994] used in the ocean model, which efficiently dampens out any vertical gradients in the mixed layer.

Especially under strong wind conditions, the surface transport of oil and other pollutants is largely governed by ocean waves. While the mean Eulerian currents are mainly driven by wave breaking, waves also induce a mean Lagrangian drift in the direction of wave propagation, the so-called Stokes drift [*Stokes*, 1847]. The GLAD drifters, whose motion reflects the cumulative effects of Eulerian current and the Stokes drift, experienced a direct hit by Hurricane Isaac on 27 August. *Curcic et al.* [2016] used the UWIN-CM forecast fields of Eulerian current and Stokes drift to simulate the GLAD trajectories during the passage of Isaac, with and without the effects of advection by waves (Figure 10). Using the Lagrangian velocity (Eulerian + Stokes) significantly improves the drifter trajectory prediction compared to the Eulerian velocity without wave effects. This indicates a high importance of the advection by Stokes drift for surface transport prediction in strong wind regimes. Following the passage of Isaac, the cold water upwelling and upper ocean mixing results in pronounced surface water density fronts (Figure 10) which are a key ingredient for the formation of submesoscale mixed-layer eddies [*Fox-Kemper et al.* 2008; *Haney et al.* 2012]. These processes were evidenced by the vigorous dispersion of GLAD drifters in the wake of Isaac [*Curcic et al.* 2016].

As can be expected based on the climatological analysis, the atmospheric forcing during SCOPE was generally stronger and features increased variability on synoptic scales (Figures 7g–7l). The turning of the winds, followed by a turning of the dominant wave direction, is a manifestation of the progression of the synoptic-scale weather systems (Figures 7i and 7l). Variability in wind speed is mirrored closely by the evolution of SWH, and features pronounced variability on time scales of a few days (Figures 7h and 7k). A potent cold front with winds of 14 m s^{-1} and SWH > 4 m, which had just passed when the realtime forecasts began, was to remain the strongest event impacting Station 42003 during the SCOPE period (Figures 7h and 7k). In addition to wave activity, surface currents respond to the stronger wind forcing during the 10–15 December period, and the local current magnitude increases to a peak value of 80 cm s^{-1}, from an average base speed of < 40 cm s^{-1} (Figure 7k). During the GLAD period, current magnitudes rarely accelerated to values > 40 cm s^{-1}, however, it is unclear whether Isaac had a more severe impact since the realtime forecasts were discontinued right after the hurricane had passed (Figure 7e).

Diurnal temperature oscillations during SCOPE were much weaker than during GLAD, but substantial air temperature swings of 8°C show the impact of cold fronts (Figures 7g and 7j). Although Station 42003 is
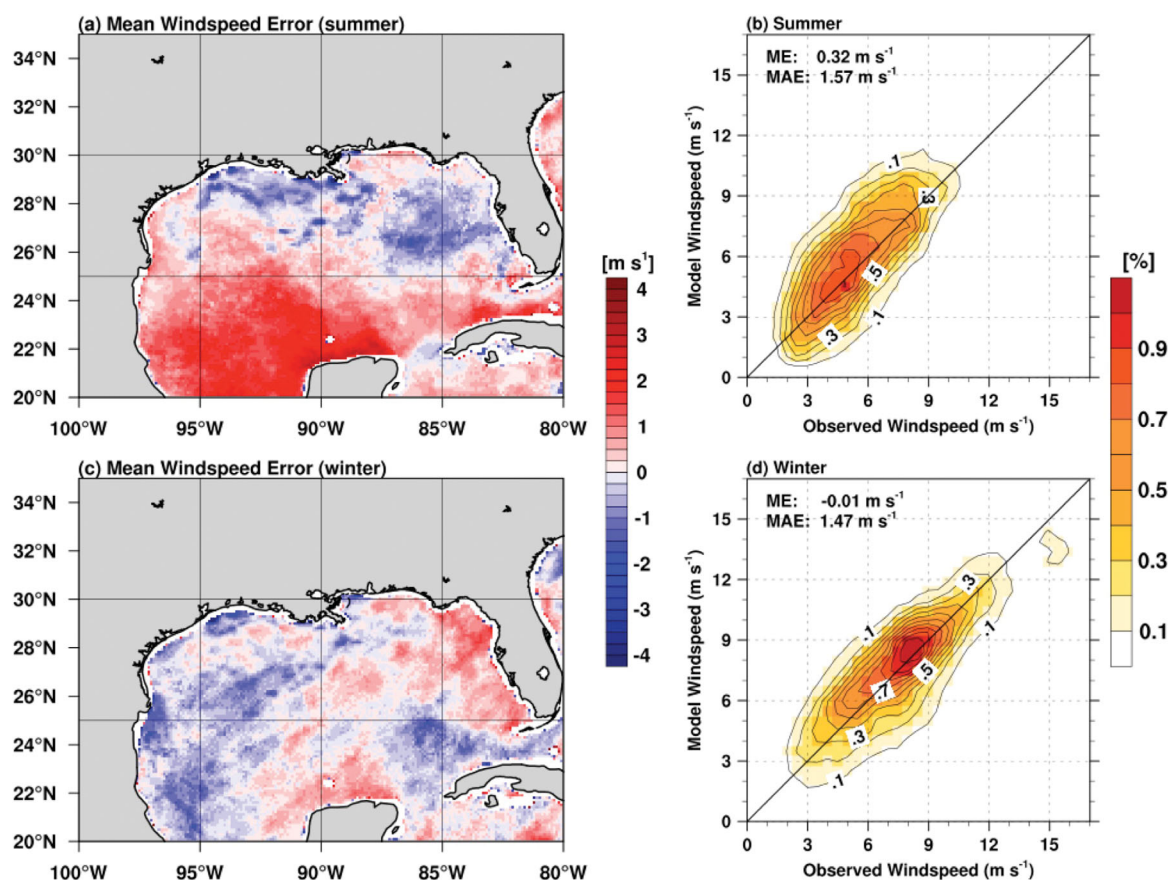
Figure 11. (left) UWIN-CM wind speed bias, averaged over the (a) GLAD and (c) SCOPE periods. (right) Frequency distributions based on the observed and predicted wind speeds from the individual 24–48 h forecasts (b: 24 July to 26 August 2012, d: 26 November to 20 December 2013).

located in the central GoM and thus subject to the moderating effect of the warm Loop Current, the difference between air and water temperature reached almost 10°C during the strongest cold outbreak, suggesting that considerable sensible heat fluxes took place during these periods. In between cold air advection events, when the area was dominated by southeasterly flow, both air and water temperature were approximately equal (Figure 7g).

4.3. Model Evaluation

The qualitative agreement between 24 and 48 h model predictions and observations in Figures 6 and 7 show that the model is able to capture the variability of the atmospheric forcing and upper ocean response. However, the model forecasts also revealed some errors and biases. For example, UWIN-CM underestimated the amplitude of the diurnal temperature cycles during relatively calm summer conditions (Figure 7a versus Figure 7d). Furthermore, during weakly forced periods, the model was also not able to reproduce much of the shorter time-scale variability in wind direction and dominant wave direction (Figure 7c versus Figure 7f).

The total amount of 35 forecasts during GLAD (22 July to 26 August 2012) and 23 forecasts during SCOPE (25 November to 18 December 2013) allowed for a quantitative analysis of model biases and errors. When averaged over the GLAD period, large part of the southern GoM featured a wind speed high bias of up to 3 m s^{-1}, whereas smaller and weaker negative wind speed bias dominated in the northern GoM regions (Figure 11a). The GoM-average model wind speed evaluation is summarized in a frequency distribution (Figure 11b), which is based on a scatter analysis of the observed and predicted wind speeds. The spatio-temporal mean wind speed bias for the entire GoM was 0.32 m s^{-1} (Figure 11b). Table 1 lists model bias and root mean square errors computed from the grid point corresponding to the location of NDBC Station 42003. The model had a slight time-mean negative air and water temperature bias, and somewhat overpredicted the wind speed at this location, which is consistent with the overall pattern (Figure 11a). In contrast,

Table 1. UWIN-CM Bias and Root Mean Squared Error During GLAD and SCOPE[a]

	Model Bias	RMSE
GLAD (1–29 Aug 2012)		
Air temperature	−0.63°C	1.07°C
Water temperature	−0.57°C	0.79°C
Wind speed	0.13 m s^{-1}	2.0 m s^{-1}
Significant wave height	−0.21 m	0.44 m
SCOPE (26 Nov 2013 to 20 Dec 2013)		
Air temperature	−0.42°C	0.81°C
Water temperature	0.18°C	0.72°C
Wind speed	0.75 m s^{-1}	1.94 m s^{-1}
Significant wave height	−0.10 m	0.32 m

[a]The model data were evaluated with observations from NDBC Station 42003. The accuracies of the NDBC instruments are ±1.0°C for air and water temperature, ±1.0 m s^{-1}, or 10% for wind speed (whichever is greater), and ±0.2 m for SWH.

the SWH bias is negative and had a magnitude of 0.21 m, which is about ∼20% of the time-mean SWH of 1 m.

The noticeable GoM-area mean high wind speed bias disappeared during the SCOPE period (Figures 11c and 11d), indicating that it may be related to physical processes dominating during weak wind regimes. In the winter, there is no coherent bias pattern, and the spatiotemporal mean bias is close to zero (Figure 11d). However, the opposite biases in the sense of overpredicted wind speed and underpredicted SWH at Station 42003 persisted (Table 1). These biases suggest that certain physical processes involving the transfer of momentum through the air-sea interface are not simulated correctly, possibly because the atmospheric and wave components of the model were developed independently. Although observed air and water temperature are approximately equal during the 5–10 December period, the model was not able to establish equality between these variables (Figures 7g and 7j). This systematic error is also reflected in the inconsistent and opposite time-mean biases of air and water temperature in Table 1 (air temperature is too cold and SST to warm). Systematic errors of this kind imply that the model produces incorrect heat fluxes.
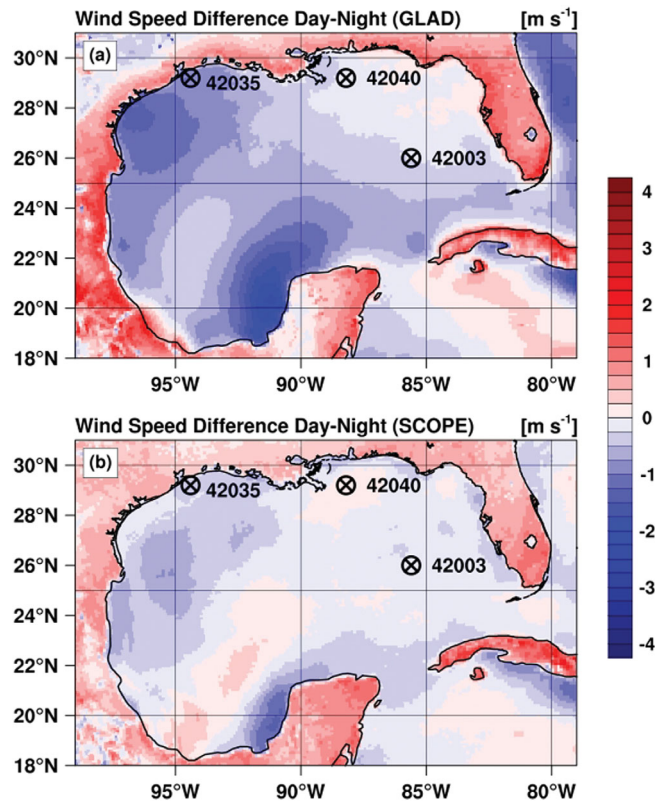

Figure 12. Differences between daytime and nighttime wind speed, averaged over the (a) GLAD and (b) SCOPE periods. Red indicates higher daytime wind speed, and blue higher nighttime wind speeds. Annotations show NDBC buoys used for the analysis of the diurnal cycle shown in Figure 13.

5. The Diurnal Cycle in Model and Observations

Noticeable diurnal temperature oscillations and, to a lesser degree, diurnal wind speed variability were presented during certain periods of the experiments (Figures 7 and 8). In this section, we investigate diurnal variability further by using both UWIN-CM predictions and long-term NDBC buoy observations from stations 42003 (1976–2014), 42040 (1995–2014), and 42035 (1993–2014).

To examine the diurnal signal in wind speed over the entire GoM, we computed the difference between the daytime (06:00–18:00 local time) and nighttime (18:00–06:00 local time) mean wind speed from the UWIN-CM forecasts. The difference fields were then averaged over the GLAD (Figure 12a) and SCOPE (Figure 12b) periods, respectively. Diurnal variability played a more prominent role during GLAD, because of the weaker large-scale wind forcing and increased summertime insolation. Generally, wind speeds were higher over land during
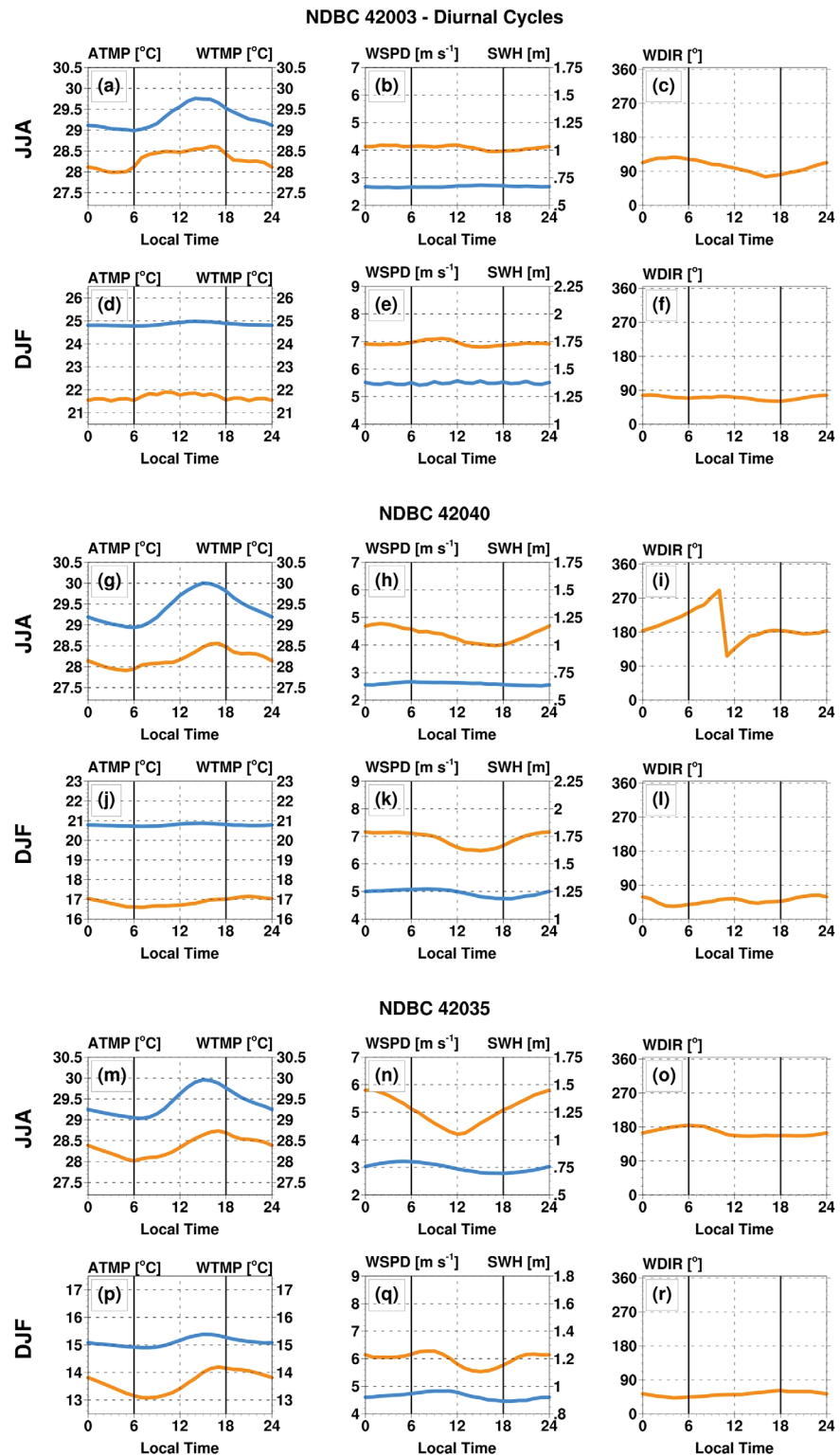
Figure 13. Diurnal cycles of (orange) atmospheric and (blue) ocean variables based on long-term observations from NDBC Stations (a–f) 42003, (g–l) 42040, and (m–r) 42035. Atmospheric variables: (left column) air temperature, (middle column) wind speed, and (right column) wind direction. Ocean variables: (left column) water temperature, and (middle column) significant wave height. The diurnal cycles for the summer period (June–August) are in Figures 13a–13c, 13g–13i, and 13m–13o, and the diurnal cycles for the winter period (December–February) are in Figures 13d–13f, 13j–13l, and 13p–13r.

the day, and higher over water at night. The daytime maximum along much of the GoM coastline is a manifestation of the sea breeze circulation. Figure 12 also reveals that the diurnal wind cycle features an interesting spatial structure. The most prominent region with higher nighttime wind speeds (diurnal amplitude of > 3 m s^{-1}) is located to the west of the Yucatán peninsula, and a secondary region with higher winds at night is in the northwestern GoM along the Texas coastline. In contrast, wind speeds in the northeastern GoM feature little diurnal variability. The pattern during SCOPE was similar, yet the magnitude of the diurnal variability was much lower, likely because the synoptic-scale forcing was stronger.

We further illustrate the spatial and seasonal variability of the diurnal cycle using observations from three NDBC buoys (Figure 13), whose locations are marked in Figure 12. All three sites feature a typical diurnal cycle in water temperature with an amplitude of $\sim 1°$C, which is weaker in the winter (Figure 13, left column). In contrast, the diurnal air temperature cycle differs between the locations, and is most pronounced at Station 42035. This buoy is also the only location that features a clear diurnal cycle during the winter (Figure 13p).

The diurnal wind speed cycles are in good agreement with the model results in Figure 12 (Figure 13, middle column). NDBC Stations 42040 and especially 42035 feature a pronounced nighttime wind speed maximum, with an amplitude of ~ 2 m s^{-1} at 42035 in the summer (Figure 13n). The diurnal variability in wind speed in the eastern GoM is much less pronounced (Figures 13b and 13e), in agreement with the model predictions during GLAD (Figure 12a). In terms of SWH, there is very little diurnal signal, except for the station close to the Texas coast, which also has the strongest diurnal wind signal (Figures 13n and 13q).

At all three buoy sites, the diurnal variability of wind direction is much more distinct during the summer (Figure 13, right column). NDBC Station 42040 (Figure 13i) features a very clear signal, which is related to the change in wind direction due to the land-sea breeze circulation. In the late morning, the wind direction switches from westerly to southeasterly. Although the sea breeze does not directly reach far into the open waters, even offshore locations show diurnal wind direction variability (Figure 13c), indicating that during the summer, diurnal wind variability is a non-negotiable factor in most of the GoM.

6. Summary and Conclusions

The main goal of this paper is to provide a comprehensive overview of the multiscale atmospheric forcing in the GoM from seasonal to diurnal time scales. Because upper ocean and atmosphere are a coupled system, accurate representations of the atmospheric forcing are crucial for the prediction of pollutants released into the environment. To better understand air-sea interaction on various time scales, we used climatologies derived from long-term observations, in situ observations from the GLAD (July/August 2012) and SCOPE (November/December 2013) field campaigns, and predictions from a next generation coupled atmosphere-wave-ocean model (UWIN-CM).

The atmospheric forcing and ocean response in the GoM feature pronounced seasonality. During the summer, large-scale winds are generally weak and exhibit little day-to-day variability. Hurricanes are rare but extreme forcing events, which impact the ocean substantially. Because of the overall weak large-scale forcing, diurnal variability is an important contributor to the forcing in the summer. Sea breeze circulations, which peak in the afternoon, affect the coastal regions, whereas nocturnal wind maxima prevail over large parts of the offshore GoM waters. Model forecasts and buoy observations revealed a complex spatial structure of the diurnal wind and temperature variability in the GoM. The forcing during the GLAD field campaign reflected the climatological conditions. Weak large-scale winds and diurnal variability prevailed throughout most of the GLAD period, except from 25–29 August 2012, when Hurricane Isaac traversed the GoM. Model predictions and in situ observations illustrated the ocean impact of Isaac's winds, which caused SWH > 5 m, strong currents, and a pronounced cold wake.

In contrast to the relatively calm summers, winters are dominated by stronger large-scale forcing and increased synoptic-scale variability. Midlatitude weather systems impact the GoM on irregular intervals (~ 3–7 days) with high winds and cold air outbreaks. There were several significant winter storm events during the SCOPE field campaign, causing strong winds (12–15 m s^{-1}), high waves (SWH > 4 m), and air temperature drops of up to 10°C. Coupled model predictions suggest that the magnitude of surface currents in the central GoM doubled from 40 to 80 cm s^{-1} during high these wind periods. Due to the stronger large-scale flow and increased synoptic-scale variability, the diurnal signal is reduced in the winter.

UWIN-CM captured the variability on seasonal, synoptic, and diurnal scales, and provided useful realtime predictions during the GLAD and SCOPE field campaigns. However, the evaluation of model forecasts with observations revealed certain biases. During the summer, the model predictions suffered from a wind speed high bias, which was most pronounced in the western GoM. This bias did not exist during SCOPE and in general, the predictions were more accurate in the winter, because the synoptic-scale evolution of winter storms is more predictable than the weak large-scale flow regime dominating in the summer. The model was also not able to predict the mixed layer characteristics after Hurricane Isaac's passage, likely due to biases in the initial conditions (mixed layer too deep). In contrast, the coupled model predicted the trajectories of GoM drifters reasonably well by accounting for the Lagrangian drift in the direction of wave propagation.

In conclusion, this study shows that the atmosphere forces the upper ocean on a wide range of time scale. Predictions of hydrocarbon transport and dispersion can be improved when the multiscale variability of the atmospheric forcing is modeled explicitly. The seasonal variability dictates how ocean and atmosphere interact on longer-time scales, but the short-term motion of oil at the ocean surface is mainly affected by synoptic-scale and diurnal variability. For example, a cold front can alleviate the potential pollution of the shoreline when the strong northerly winds induce an offshore transport that pushes the oil away from the shore. In contrast, the onshore flow due to the sea breeze during a clear summer day could cause the opposite effect. Next generation coupled atmosphere-wave-ocean model are able to capture the observed multi-scale variability in the atmospheric forcing, and are thus an integral aspect in predicting the fate of pollutants during [6/14] possible future oil spills. Future advancements in representing physical processes and reducing the biases of forecast models will be necessary to further improve predictions.

References

Appendini, C. M., A. Torres-Freyermuth, P. Salles, J. López-González, and E. T. Mendoza (2014), Wave climate and trends for the Gulf of Mexico: A 30-yr wave hindcast, *J. Clim.*, *27*(4), 1619–1632, doi:10.1175/JCLI-D-13-00206.1.

Berg, R. (2013), *Tropical Cyclone Report Hurricane Isaac (AL092012)*. Natl. Hurricane Cent., Miami, Fla.

Chang, Y.-L., and L.-Y. Oey, (2010a), Why can wind delay the shedding of Loop Current eddies?, *J. Phys. Oceanogr. 40*, 2481–2495, doi: 10.1175/2010JPO4460.1.

Chang, Y.-L., and L.-Y. Oey, (2010b), Eddy and wind-forced heat transports in the Gulf of Mexico, *J. Phys. Oceanogr. 40*, 2728–2742, doi: 10.1175/2010JPO4474.1.

Chang, Y.-L., and L.-Y. Oey (2012), Why does the Loop Current tend to shed more eddies in summer and winter?, *Geophys. Res. Lett.*, *39*, L05605, doi:10.1029/2011GL050773.

Chen, S. S., and M. Curcic (2015), Ocean surface waves in Hurricane Ike (2008) and superstorm sandy (2012): Coupled model predictions and observations, *Ocean Modell.*, *103*, 1–16, doi:10.1016/j.ocemod.2015.08.005.

Chen, S. S., W. Zhao, M. a. Donelan, J. F. Price, and E. J. Walsh (2007), The CBLAST-hurricane program and the next-generation fully coupled atmosphere–wave–ocean models for hurricane research and prediction, *Bull. Am. Meteorol. Soc.*, *88*(3), 311–317, doi:10.1175/BAMS-88-3-311.

Chen, S. S., W. Zhao, M. a. Donelan, and H. L. Tolman (2013), Directional wind–wave coupling in fully coupled atmosphere–wave–ocean models: Results from CBLAST-hurricane, *J. Atmos. Sci.*, *70*(10), 3198–3215, doi:10.1175/JAS-D-12-0157.1.

Coelho, E. F. et al. (2015), Ocean current estimation using a multi-model ensemble Kalman filter during the Grand Lagrangian Deployment experiment (GLAD), *Ocean Modell.*, *87*, 86–106, doi:10.1016/j.ocemod.2014.11.001.

Curcic, M., S. S. Chen, and T. M. Özgökmen (2016), Hurricane-induced ocean waves and stokes drift and their impacts on surface transport and dispersion in the Gulf of Mexico, *Geophys. Res. Lett.*, *43*, 2773–2781, doi:10.1002/2015GL067619.

de Velasco, G. G., and C. D. Winant (1996), Seasonal patterns of wind stress and wind stress curl over the Gulf of Mexico, *J. Geophys. Res.*, *101*, 18,127–18,140, doi:10.1029/96JC01442.

DiMego, G. J., L. F. Bosart, and G. W. Endersen (1976), An examination of the frequency and mean conditions surrounding frontal incursions into the Gulf of Mexico and Caribbean Sea, *Mon. Weather Rev.*, *104*(6), 709–718, doi:10.1175/1520-0493(1976)104<0709:AEOTFA>2.0.CO;2.

Donelan, M. A., M. Curcic, S. S. Chen, and A. K. Magnusson (2012), Modeling waves and wind stress, *J. Geophys. Res.*, *117*, C00J23, doi:10.1029/2011JC007787.

Eichler, T., and W. Higgins (2006), Climatology and ENSO-related variability of North American extratropical cyclone activity, *J. Clim.*, *19*(1981), 2076–2093, doi:10.1175/JCLI3725.1.

Fox-Kemper, B., R. Ferrari, and R. Hallberg (2008), Parameterization of mixed layer eddies. Part I: Theory and diagnosis, *J. Phys. Oceanogr.*, *38*, 1145–1165, doi:10.1175/2007JPO3792.1.

Gray, W. M. (1984), Atlantic seasonal hurricane frequency. Part I: El Niño and 30 mb Quasi-biennial oscillation influences, *Mon. Weather Rev.*, *112*(9), 1649–1668, doi:10.1175/1520-0493(1984)112<1649:ASHFPI>2.0.CO;2.

Haney, S., S. Bachman, B. Cooper, S. Kupper, K. McCaffrey, L. V. Roekel, S. Stevenson, B. Fox-Kemper, and R. Ferrari (2012), Hurricane wake restratification rates of one-, two- and three-dimensional processes, *J. Mar. Res.*, *70*, 824–850, doi:10.1357/002224012806770937.

Jaimes, B., and L. K. Shay (2009), Mixed layer cooling in mesoscale oceanic eddies during Hurricanes Katrina and Rita, *Mon. Weather Rev.*, *137*(12), 4188–4207, doi:10.1175/2009MWR2849.1.

Jaimes, B., L. K. Shay, and G. R. Halliwell (2011), The Response of Quasigeostrophic Oceanic Vortices to Tropical Cyclone Forcing, *J. Phys. Oceanogr.*, *41*(10), 1965–1985, doi:10.1175/JPO-D-11-06.1.

Large, W. G., J. C. McWilliams, and S. C. Doney (1994), Oceanic vertical mixing: A review and a model with a nonlocal boundary layer parameterization, *Rev. Geophys.*, *32*, 363–403, doi:10.1029/94RG01872.

Lee, C.-Y., and S. S. Chen (2012), Symmetric and asymmetric structures of hurricane boundary layer in coupled atmosphere–wave–ocean models and observations, *J. Atmos. Sci.*, *69*(12), 3576–3594, doi:10.1175/JAS-D-12-046.1.

Lee, C.-Y., and S. S. Chen (2014), Stable Boundary Layer and Its Impact on Tropical Cyclone Structure in a Coupled Atmosphere–Ocean Model, *Mon. Weather Rev.*, *142*(5), 1927–1944, doi:10.1175/MWR-D-13-00122.1.

Levinson, D. H., P. J. Vickery, and D. T. Resio (2009), A climatology of landfalling hurricane central pressures along the Gulf of Mexico Coast, in *11th International Workshop on Wave Hindcasting and Forecasting and 2nd Coastal Hazard Symposium*, Halifax, Nova Scotia, Canada.

Mendoza, V. M., E. E. Villanueva, and J. Adem (2005), On the annual cycle of the sea surface temperature and the mixed layer depth in the Gulf of México, *Atmosfera*, *18*(2), 127–148.

Nowlin, W. D., and C. A. Parker (1974), Effects of a cold-air outbreak on shelf waters of the Gulf of Mexico, *J. Phys. Oceanogr.*, *4*(3), 467–486, doi:10.1175/1520-0485(1974)004 < 0467:EOACAO>2.0.CO;2.

Nowlin, W. D., A. E. Jochens, S. F. DiMarco, R. O. Reid, and M. K. Howard (2005), Low-frequency circulation over the Texas-Louisiana continental shelf, in *Circulation in the Gulf of Mexico: Observations and Models*, vol. 161, edited by W. Sturges and A. Lugo-Fernandez, pp. 219–240, AGU, Washington, D. C.

Oey, L.-Y. (1995), Eddy- and wind-forced shelf circulation, *J. Geophys. Res.*, *100*, 8621–8637, doi:10.1029/95JC00785.

Özgökmen, T. M., et al. (2014), Research overview of the consortium for advanced research on transport of hydrocarbon in the environment (CARTHE), in *International Oil Spill Conference Proceedings*, vol. 2014, pp. 544–560, Savannah, Georgia.

Poje, A. C. et al. (2014), Submesoscale dispersion in the vicinity of the Deepwater Horizon spill, *Proc. Natl. Acad. Sci. U. S. A.*, *111*(35), 12,693–12,698, doi:10.1073/pnas.1402452111.

Price, J. F. (1981), Upper ocean response to a hurricane, *J. Phys. Oceanogr.*, *11*(2), 153–175, doi:10.1175/1520-0485(1981)011 < 0153:UORTAH>2.0.CO;2.

Price, J. F., T. B. Sanford, and G. Z. Forristall (1994), Forced stage response to a moving hurricane, *J. Phys. Oceanogr.*, *24*(2), 233–260, doi:10.1175/1520-0485(1994)024 < 0233:FSRTAM>2.0.CO;2.

Smith, T. A., S. Chen, T. Campbell, P. Martin, W. E. Rogers, S. Gaberšek, D. Wang, S. Carroll, and R. Allard (2013), Ocean–wave coupled modeling in COAMPS-TC: A study of Hurricane Ivan (2004), *Ocean Modell.*, *69*, 181–194, doi:10.1016/j.ocemod.2013.06.003.

Stokes, G. G. (1847), On the theory of oscillatory waves, *Trans. Cambrige Philos. Soc.*, *8*, 441–473.

Sybrandy, A. L., P. P. Niiler, C. Martin, W. Scuba, E. Charpentier, D. T. Meldrum (2009), Global Drifter Programme: Barometer Drifter Design Reference, *DBCP Rep. 4*, Data Buoy Coop. Panel, Ramonville-Saint-Aigne, France.

Villanueva, E. E., V. M. Mendoza, and J. Adem (2010), Sea surface temperature and mixed layer depth changes due to cold-air outbreak in the Gulf of M??xico, *Atmosfera*, *23*(4), 325–346.

Wang, W., W. D. Nowlin, and R. O. Reid (1998), Analyzed surface meteorological fields over the northwestern Gulf of Mexico for 1992–94: Mean, seasonal, and monthly patterns, *Mon. Weather Rev.*, *126*(11), 2864–2883, doi:10.1175/1520-0493(1998)126 < 2864:ASMFOT>2.0.CO;2.

Xu, F., Y. Chang, L. Oey, and P. Hamilton (2013), Loop current growth and eddy shedding using models and observations: Analyses of the July 2011 eddy-shedding event, *J. Phys. Oceanogr. 43*, 1015–1027, doi:10.1175/JPO-D-12-0139.1.

Zavala-Hidalgo, J., R. Romero-Centeno, A. Mateos-Jasso, and S. L. Morey (2014), The response of the Gulf of Mexico to wind and heat flux forcing: What has been learned in recent years?, *Atmosfera*, *27*(3), 317–334.

Erratum

In the originally published version of this article, there were several typos within the body of the manuscript as well as an omission in the acknowledgment section. These instances have since been corrected. This version may be considered the authoritative version of record.